Hindawi
Advances in Civil Engineering
Volume 2020, Article ID 3784271, 16 pages
https://doi.org/10.1155/2020/3784271

Research Article

Numerical Theoretical Study on Mechanical Properties of New Reinforced Tenon Precast Shear Walls

Wei Chen,[1] Qing Wu,[1] Dongyue Wu,[1] Longji Dang,[2] and Feifei Jiang[1]

[1]*School of Civil Engineering and Architecture, Jiangsu University of Science and Technology, Zhenjiang, Jiangsu, China*
[2]*School of Civil Engineering, Southeast University, Nanjing, Jiangsu, China*

Correspondence should be addressed to Qing Wu; wuqing@just.edu.cn

Received 2 January 2020; Revised 30 August 2020; Accepted 13 September 2020; Published 14 October 2020

Academic Editor: Rosario Montuori

Precast construction technologies have several advantages in industrialized production, such as quality control and energy conservation. However, the joint interface slippage between the precast components causes detrimental effect on the mechanical properties, such as dowel shear stress on the connecting steel bars, which strictly restricts the development of assembly technology in aseismic structure. In order to eliminate the horizontal slippage along the assemble joint and optimize the mechanical performance of horizontal joint connections, a new reinforced tenon joint precast shear wall is proposed in this paper. Finite element numerical simulations are conducted on three reinforced tenon joint specimens and a reference specimen to understand the mechanical properties of the reinforced tenon and boundary confinement components of shear wall. The load-displacement curves, the equivalent plastic strain distribution diagram, and the concrete damage distribution diagram are obtained. It is found that the boundary components provide bending strength and the reinforced tenon can reduce the harmful influence of dowel-action shear stress on longitudinal connecting reinforcements. Therefore, the bending and shearing forces are separated at the joint interface. Based on the numerical simulation results and the calculation theory of normal section bearing capacity, the theoretical calculation bending capacity formula of reinforced tenon precast shear wall is established. The obtained calculation results are in good agreement with the simulation results and can accurately reflect the bending capacity of the jointed interface.

1. Introduction

Currently, precast concrete structures are widely used as alternatives to the common cast in situ structures in many architectural forms. The use of precast concrete structures has rapidly increased due to the enhanced features that they possess, such as construction speed, high quality control, and lower levels of construction waste [1]. The reinforced concrete shear walls have widely been used for high-rise buildings in seismic regions in China because of the high lateral strength and stiffness [2]. The combination of precast concrete technology and shear wall structures enables the shear wall structure construction to achieve both high lateral force resistance and highly construction speed.

The joints of precast concrete shear walls, as an important part, strongly affect the performance of entire structure. In recent decades, many scholars have studied the behavior and influence of the connecting joint [3]. Jiaru et al. [4] used grout sleeves to connect the precast shear walls and demonstrated that the stresses on the vertical reinforcements could be effectively forced by the grout sleeves. Lu et al. [3] and Jiaru et al. [5] used the joint connecting beams to connect the top and the bottom walls, and their study results proved that after the peak of horizontal force, the specimen had an in-plane slide between the precast wall and the cast-in-place part.

Many early studies focused on the traditional straight precast joint have indicated that [6–9] when the joints cracked and slipped, the vertical connecting steel bars are typically required to bear the shear stress resulted from the dowel action [10]. The dowel action of steel bars provides a part of the shear capacity of the joints at the cost of reducing the yielding strength of the connection reinforcements. Early studies have also proved [8] that both the joint gap opening

and the interface slip have significant influence on the lateral shear capacity of the connection reinforcements. Moreover, the influence trends and the degrees of joint gap opening and slip are different as shown in Figures 1 and 2. The above discussion indicates that it is unreliable and harmful to utilize the connection reinforcements to represent the shear resistance components, which still widely exists in common straight precast joint. In this case, many scholars have proved that the tenon shear keys can be used to improve the mechanical performance of the joint surface. Foerster et al. [11] proved that the ultimate shear strength of the tooth-grooved interface was 40% and the ductility was 65% higher than those of straight interfaces. Soudki et al. [12] found that the tooth-grooved connections could improve the seismic performance of precast shear walls 300% for the straight interface maximum shear bearing capacity and 40% for the ultimate shear bearing capacity. However, there are also some defects in tooth-grooved joint interface. Xizhi et al. [13] carried out quasi-static loading tests on two tooth-grooved connections precast shear wall specimens and demonstrated that the tooth-grooved joint specimens were not strong enough and suddenly cut off after the ultimate load mainly because the tooth-grooves were small and made up of plain concrete, poor ductility, and limited shear resistance. Xizhi et al. [14] conducted monotonic push-over tests on eight 1/2-scaled tooth-grooved connection specimens and concluded that the number of the tooth-grooved joints had small influence on their shear bearing capacity. Therefore, as long as the number and the strength of the grooves can resist the shear force borne by the cross section, there is no need to arrange it along the whole joint.

In this paper, a new reinforced tenon connection joint for precast shear wall is proposed to relieve the influence of dowel action on the mechanical performance of precast shear wall. Figures 3 and 4 illustrate the construction and reinforcement layout plan of the precast shear wall with the proposed reinforced tenon, respectively. A large groove is placed near the bending neutral axis at the bottom of the wall panel to form the reinforced tenon joint, and the vertical distributed connecting bars in the groove are disconnected. In this case, the strength of the shear wall is adjusted by enhancing the vertical reinforcements in the boundary confinement columns. Once the top and the bottom walls are hoisted in place, the reinforcement steel cage with the postpoured concrete is set in the groove to complete the reinforced tenon joint. In addition, the vertical connecting steel bars of boundary confinement columns are anchored by grouting.

The enhanced reinforcement cage in the tenon can significantly reduce the horizontal slips at the joint interface and provide effective bending and shearing capacity. Moreover, it can separate the bending and shearing forces onto the boundary confinement column and the reinforced tenon, respectively. The reinforced tenon provides shear resistance, while the boundary confinement columns provide flexural bearing advantages. The two components cooperatively improve the bearing capacity of the joint surface. Furthermore, the concept is simple and clear and adopts traditional and convenient construction techniques, which can accelerate the speed and reduce the cost of construction.

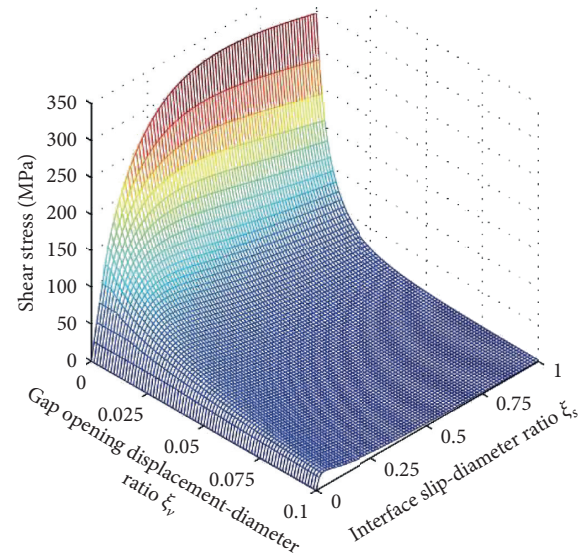

Figure 1: The space curved surface of ξ_s and ξ_v against shear stress of single steel bar. ξ_s is the interface slip-diameter ratio; ξ_v is the vertical gap opening displacement-diameter ratio.

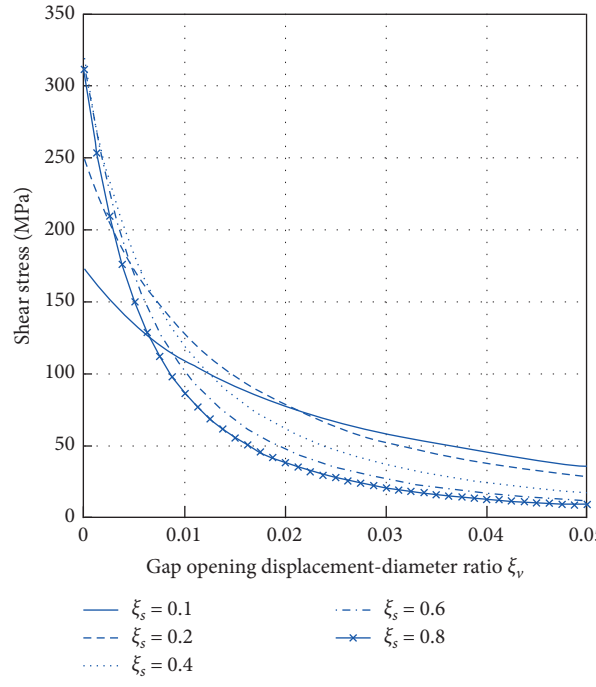

Figure 2: The curve of ξ_v against shear stress of single steel bar with different ξ_s. ξ_s is the interface slip-diameter ratio; ξ_v is the vertical gap opening displacement-diameter ratio.

In order to understand the mechanical performance and verify the effectiveness and rationality of the new reinforced tenon joint precast shear wall, this paper analyzes three precast shear walls with different shear span ratios and one common flat-seam joint.

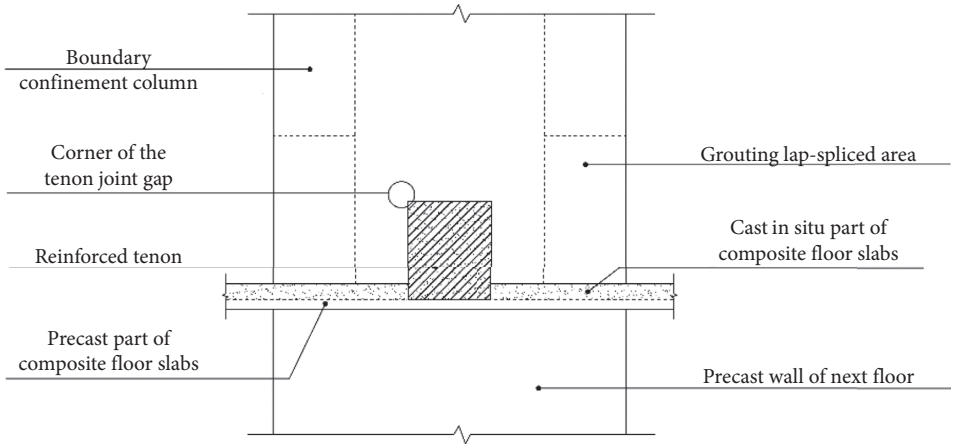

Figure 3: Construction of precast shear wall with the proposed reinforced tenon.

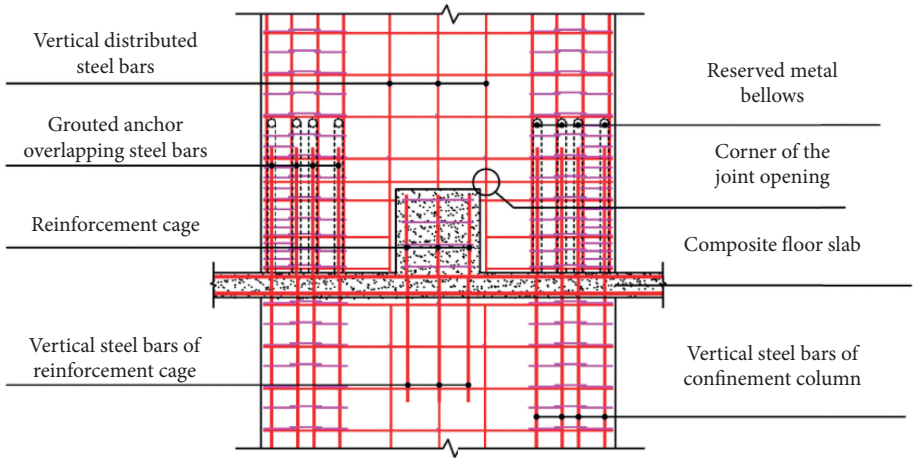

Figure 4: Reinforcement layout plan of precast shear wall with the proposed reinforced tenon.

2. Finite Element Models

2.1. Specimens. In order to verify the mechanical performance of the reinforced tenon joint connection, four finite element specimen models are established and identified as SW1, TSW1, TSW2, and TSW3. SW1 is the common flat-seam joint specimen as the contrast component with a shear span ratio of 1.5. TSW1, TSW2, and TSW3 are three reinforced tenon joint precast specimens with shear span ratios of 1.0, 1.5, and 2.0, respectively. The design parameters of four specimens were determined according to the "Code for design of concrete structures" (GB 50010-2010) [15]. As shown in Figure 5(b), 8C16 (eight steel bars with diameter of 16 mm) are used as the vertical reinforcements in the boundary area at wall toes of all specimens, 6C12 (six steel bars with diameter of 12 mm) are set as the vertical reinforcements out of the boundary area, and C10 (diameter is 10 mm) horizontal closed-loop reinforcements are used as horizontal distribution bars at the wall center spaced at constant intervals of 200 mm. As shown in Figure 5(a), the loading beam (1750 mm long × 250 mm deep × 240 mm thick) provides anchorage for the vertical load, and the foundation beam (2500 mm long × 650 mm deep × 700 mm thick) provides a rigid base. C35 concrete (China standard, the standard value of cubic compressive strength and the design value of compressive strength at the test day were 35 MPa and 16.7 MPa, respectively) and HRB400 (China standard, the standard and the design values of yield strength were 400 MPa and 360 MPa, respectively) mild steel bars were used for all specimens. Table 1 lists the parameters of reinforcement configuration for the four specimens.

2.2. Material Properties. In this study, the ABAQUS finite element simulation software was utilized to simulate the nonlinear static behavior of the reinforced tenon joint precast shear wall. The concrete damaged plasticity (CDP) model in ABAQUS was utilized to simulate the stiffness degradation of concrete under seismic loading. The elastic modulus of concrete was replaced by the secant modulus in the CDP model [16, 17], which is defined as the secant slope from the origin of the curve to the point of $0.45f_c$.

The uniaxial compressive and the tensile constitutive behaviors of the concrete materials are required to define the CDP model in ABAQUS. Figure 6 shows the plastic damage evolution and the stiffness recovery of concrete under

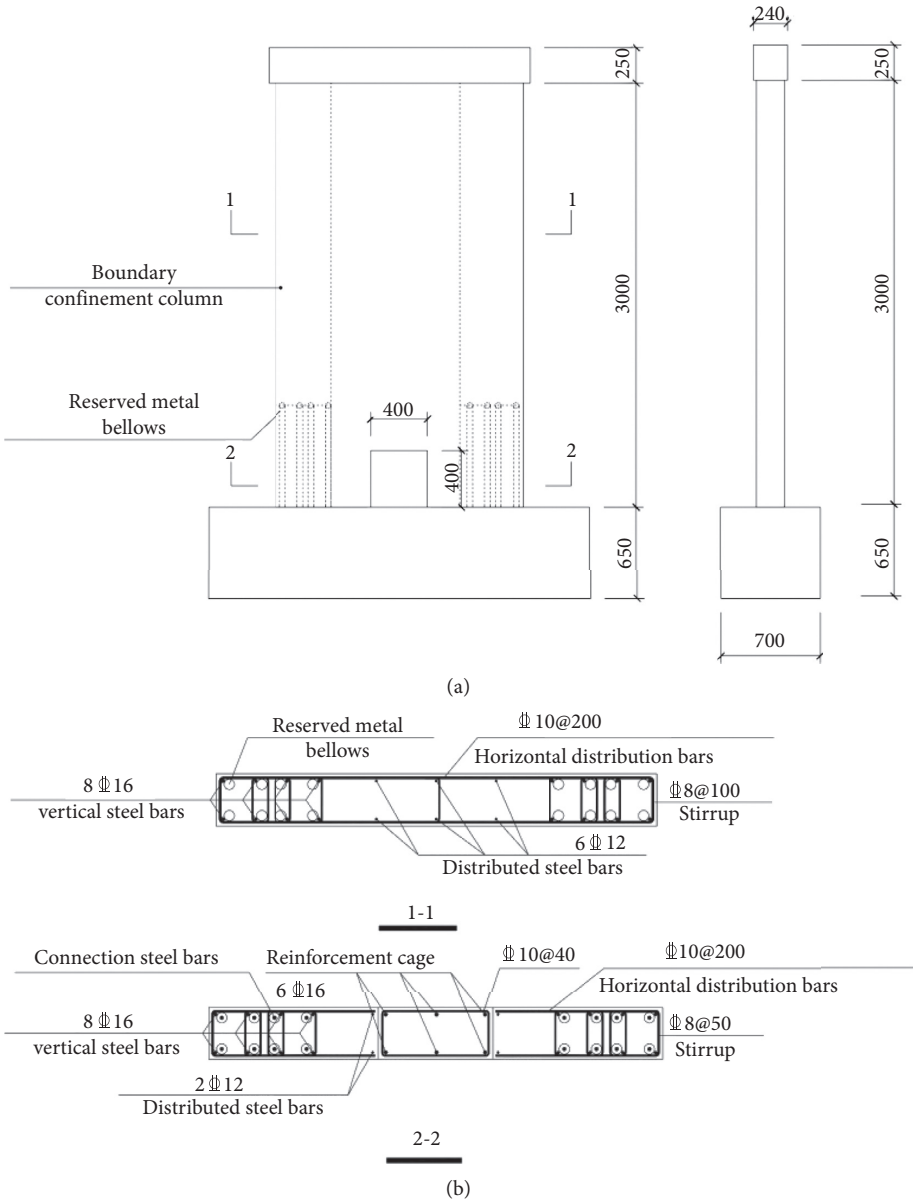

Figure 5: Dimensions of the specimen: (a) outline dimensions of the model; (b) cross section details of 1-1 and 2-2.

Table 1: Reinforcement configuration parameters of four specimens.

Specimen	Width, l_w (mm)	Thickness, b_w (mm)	Height, h_w (mm)	Shear span ratio, h_w/l_w	Reinforced tenon size	Stirrup	Horizontal distribution bars	Reinforcement cage
SW1	1700	200	2550	1.5	—	C8 @100/50	C10@200	6C16 C10@100
TSW1	1700	200	1700	1	400 × 400			
TSW2	1700	200	2550	1.5	400 × 400			
TSW3	1700	200	3400	2	400 × 400			

uniaxial reciprocating load in the CDP model. The plastic damage evolution and the stiffness recovery of concrete can be calculated from the following two formulas, respectively [16, 18]:

$$\sigma_t = (1 - d_t)E_c\left(\varepsilon_t - \tilde{\varepsilon}_t^{pl}\right), \quad (1)$$

$$\sigma_c = (1 - d_c)E_c\left(\varepsilon_c - \tilde{\varepsilon}_c^{pl}\right), \quad (2)$$

Table 2: Parameters for ABAQUS material definition of concrete.

Parameter	Taken value	Description
Ψ	32	Dilation angle
e	0.1	Eccentricity
f_{b0}/f_{c0}	1.16	The ratio of initial equibiaxial compressive yield stress to initial uniaxial compressive yield stress
K	0.6667	K_C, the ratio of the second stress invariant on the tensile meridian
μ	0.005	Viscosity parameter

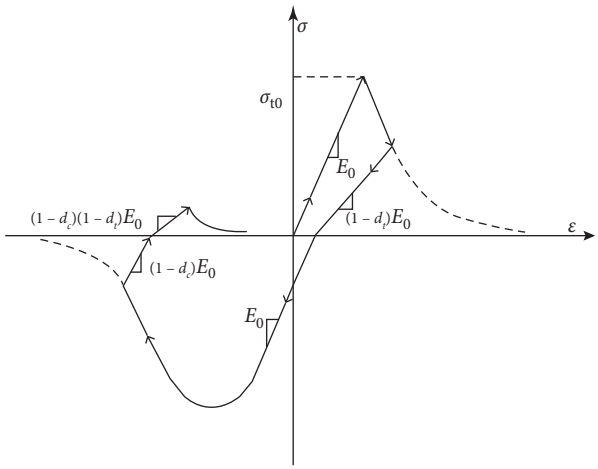

Figure 6: A single, uniaxial tensile-compressive loading cycle.

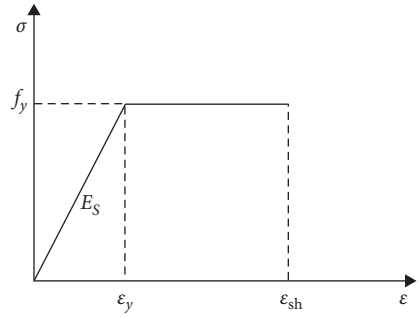

Figure 7: Constitutive model for reinforcing bar.

where E_c is the initial elastic stiffness; $\tilde{\varepsilon}_c^{pl}$ and $\tilde{\varepsilon}_t^{pl}$ are the plastic strains for compression and tension, respectively; and d_t and d_c are the two independent uniaxial compressive and tensile damage variables, respectively, defined in the CDP model [19, 20]. The expressions of the damage factor can be found in the China Code for design of concrete structures (GB 50010-2010) [15]. The CDP model follows the isotropic assumption, where the elastic damage combined with tension and compression plasticity was used to replace the inelastic behavior of concrete. The damage factor D in [15] cannot be directly used in the CDP model. However, it can be transformed into plastic damage factor d according to the following formula:

$$d = 1 - (1 - D)^{0.5}. \quad (3)$$

Other parameters considered in the CDP model in this study are listed in Table 2.

The elastic and inelastic stress-strain relationships for reinforcement steel are used. The constitutive model of the reinforcing bar adopting the ideal elastic-plastic two-fold line model is shown in Figure 7.

2.3. Element Type. In order to realistically simulate the complex stress of reinforcing bars in the joint interface, which composites tension and shear forces, the beam element "B31" is used [21]. On the contrary, truss element "T3D2" is used to simulate the remaining reinforcements in order to improve the calculation efficiency. The concrete and the grouting materials adopt a three-dimensional solid element "C3D8R," and the size of each concrete element is 100 mm. Figures 8(a) and 8(b) show the finite element models of shear wall and reinforcement bars.

2.4. Joint Simulation and Boundary Conditions. The key of establishing the reinforced tenon joint precast shear wall model is the simulation of the joint between the upper and the lower wall panels. The finite element model is mainly composed of upper and lower solids, as shown in Figure 8. The upper solid is composed of wall panel and a loading beam, while the lower solid is composed of reinforced tenon and foundation beam. Many studies have shown that it is more reasonable to adopt surface-to-surface contact model to simulate the concrete joint interface friction and compression [22, 23], which includes vertical and tangential behaviors. The vertical behavior is defined as "hard" contact, and the separation is allowed. When the contact surfaces are under compression, 100% pressure can be transmitted through the contact surface, but the constraint will be invalid when the stress turns to tension [24]. The tangential behavior is defined as friction contact, and no slip occurred when the joint interface shear stress is smaller than the static friction strength. However, slip is allowed when the shear stress is larger than the static friction strength and the surface friction stress is equal to the static friction strength with static friction ratio of 0.4 [22]. The interaction between concrete and steel bars is defined as "embedded region," because the slip between concrete and steel bars is ignored.

2.5. Loading Process. Constant axial load and increasing lateral displacements were applied to the walls. The walls were tested with an axial compression ratio of 0.1, and the increasing cyclic lateral displacement is shown in Figure 9. The lower beam was fixed to the laboratory floor to provide reaction force and ensure that the specimens were not slip during loading.

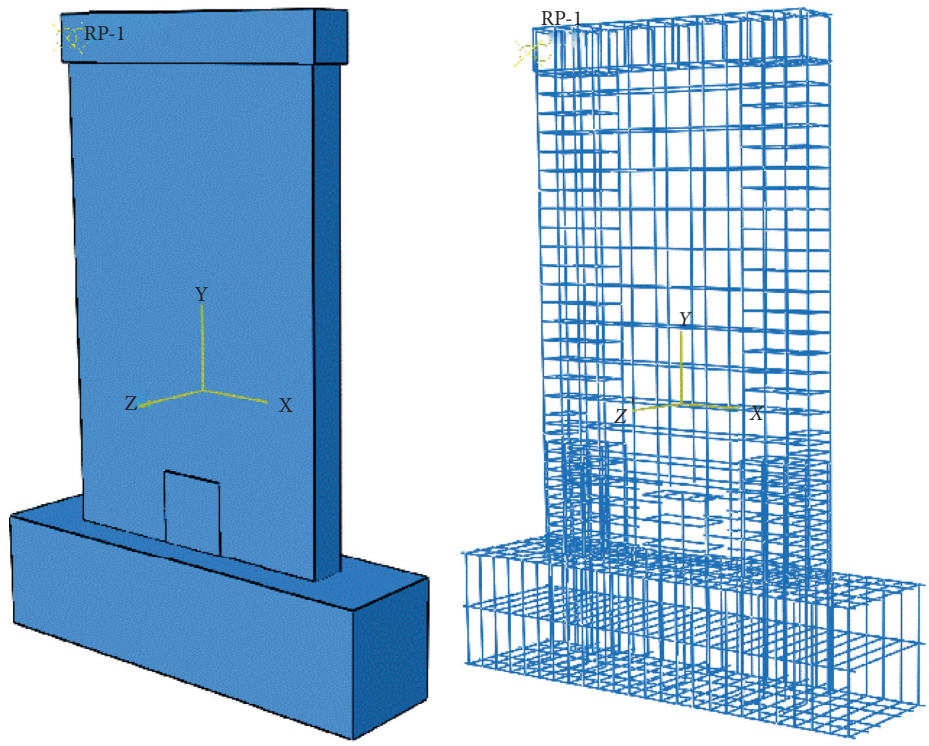

Figure 8: Finite element models: (a) shear wall; (b) reinforcement bars.

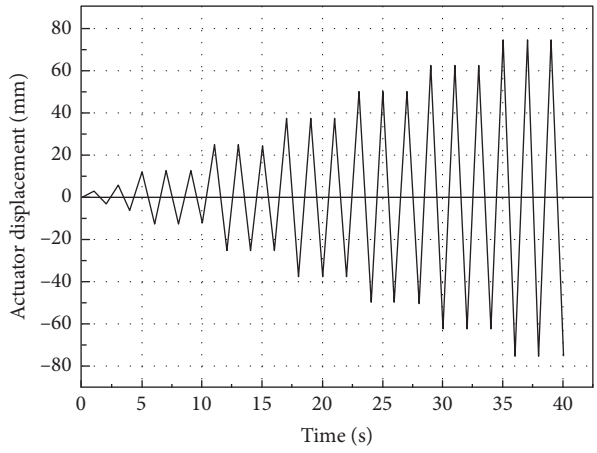

Figure 9: The increasing lateral displacement.

2.6. Verification of Finite Element Simulation Results. The effectiveness and the accuracy of the finite element modeling technique were validated by comparing the simulation results with the experimental specimens RHC-2 in [25]. The experimental specimen was tested as shown in Figure 10. The dimensions and the reinforcement configuration of the RHC-2 are shown in Figure 11. The cross section of shear wall was 1700 mm wide, 3400 mm height, and 200 mm thick. The precast wall panel was connected with foundation beam by using the grouting metal bellow.

The test setup shown in Figure 10(b) was constructed considering the equipment including concrete reaction wall, hydraulic jacks, hydraulic actuator, screw stem, steel girder, and steel strand. Cyclic lateral loads were applied by a 1000 kN hydraulic servo control system mounted to the reaction wall. Vertical load was applied by two hollow core jacks placed on the top of the specimen with two prestressed steel strands. Moreover, two steel beams with rollers were fixed on the reaction frame to prevent the tilting of the specimens during the test.

According to the constitutive relationship of the materials and the element type mentioned above, the finite element model of RHC-2 was established. Figure 12 shows that the damages of test and simulation occur in the same position and both appear at the bottom edge of the shear wall. Figures 13(a) and 13(b) show the lateral force-top displacement hysteresis curves and the skeleton curves, respectively, of both the simulation model and the experimental specimen under displacement control. The simulation curves show good agreement with the experiment curves before yielding. In the positive and negative loading directions, the experimental lateral load in the vicinity of peak point is slightly larger than the simulated one, and the residual displacement is smaller. The yielding lateral load of experimental specimen and the simulated model are 540 kN and 570 kN, respectively, with an error of 5.5%. The maximum lateral loads of experimental specimen and the simulated model are 697 kN and 650 kN, respectively, with an error of 6.7%. In general, good agreement between the simulation and the experimental results is achieved for the specimens.

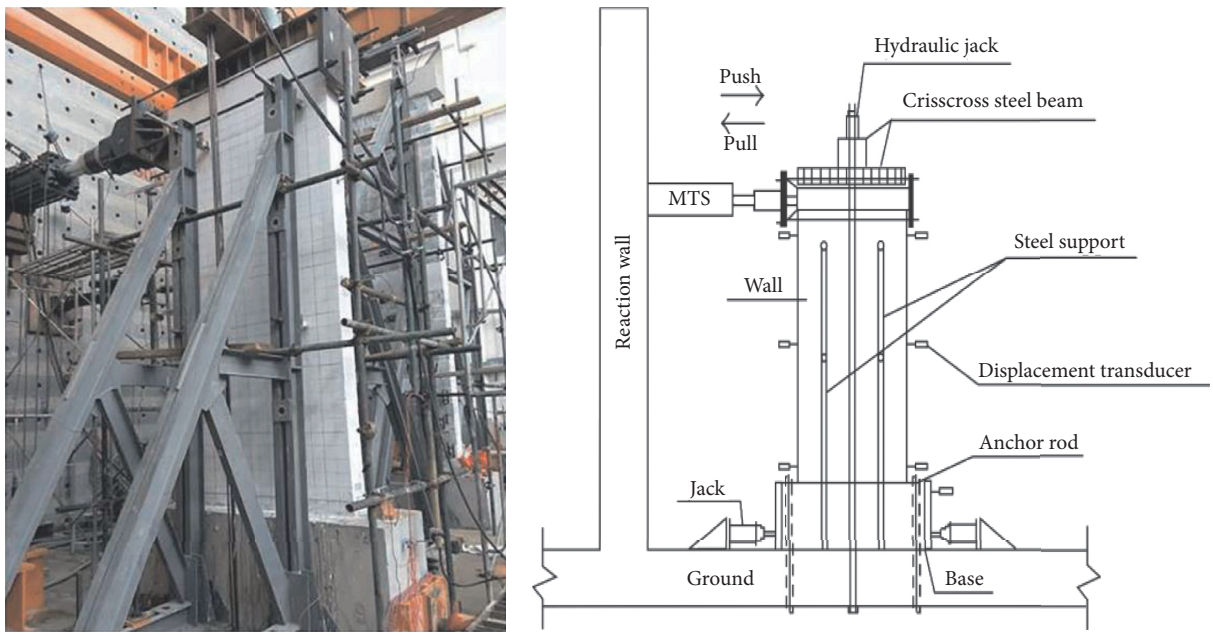

Figure 10: (a) Experimental specimen picture; (b) test setup.

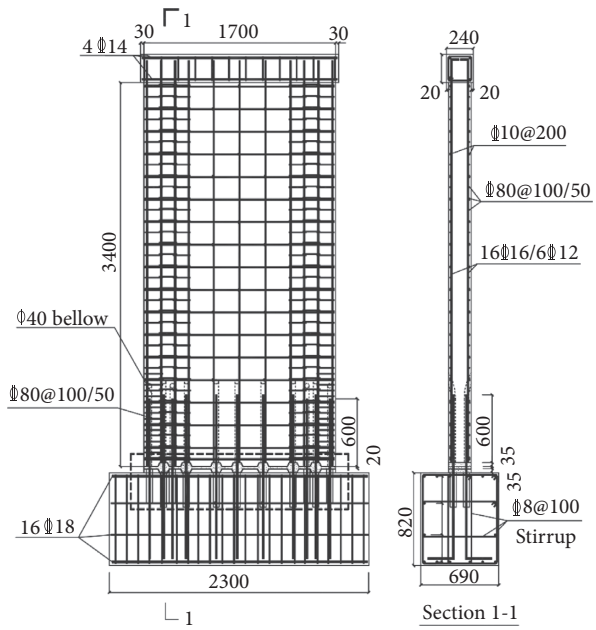

Figure 11: Dimensions (mm) and reinforcement configuration of the test specimen.

3. Simulation Results

3.1. Load-Displacement Curve. The measured load-displacement and skeleton curves of four specimens are shown in Figure 14. Overall, the reinforced tenon joint and the common flat-seam joint specimen have similar hysteretic curves. Before yielding, the specimens are in the elastic stage and the curves are approximately linear, and the residual deformations are small. After yielding, the hysteretic loops start to incline to the displacement axis. The area of the hysteretic loops increases and becomes plump. After unloading, the residual deformation becomes large and the hysteretic curves no longer overlap, which means that the specimens are in the elastic-plastic stage and demonstrate good energy consumption capacity. After the peak load, the load decreases, and the hysteretic loops exhibit pinching phenomenon.

For SW1, and TPW2, the skeleton curves are basically in coincidence with each other, especially, before the peak load. This indicates that the reinforced tenon joint connection can effectively bear and transfer the force. In specimens TSW1, TSW2, and TSW3, no significant strength and stiffness degradation occur during the cyclic loading. However, obvious strength degradation is observed from the hysteretic curves of SW1 at the second-to-last cyclic loading, mainly caused by the slip between the wall panel and the foundation beam. Inspection of skeleton curves indicates that the load-bearing capacity and the ductility of specimens improve when the aspect ratio of reinforced tenon shear wall ranges from 1 to 2.

3.2. Damage Distribution and Failure Mechanisms. The equivalent plastic strain distribution diagram (PEEQ) and tensile damage distribution diagram (DAMAGET) of each specimen at the ultimate load situation are shown in Figures 15 and 16, respectively.

Equivalent plastic strain (PEEQ) is utilized to assess the cumulative plastic strain of the specimens. When the PEEQ coefficient is higher than 0, the materials are yielded. Figure 15 shows that the PEEQ distributions of reinforce tenon specimens TSW1-3 are similar and the plastic strain is embracing around the reinforce tenon. However, the height of plastic strain area changes with the variation of shear span

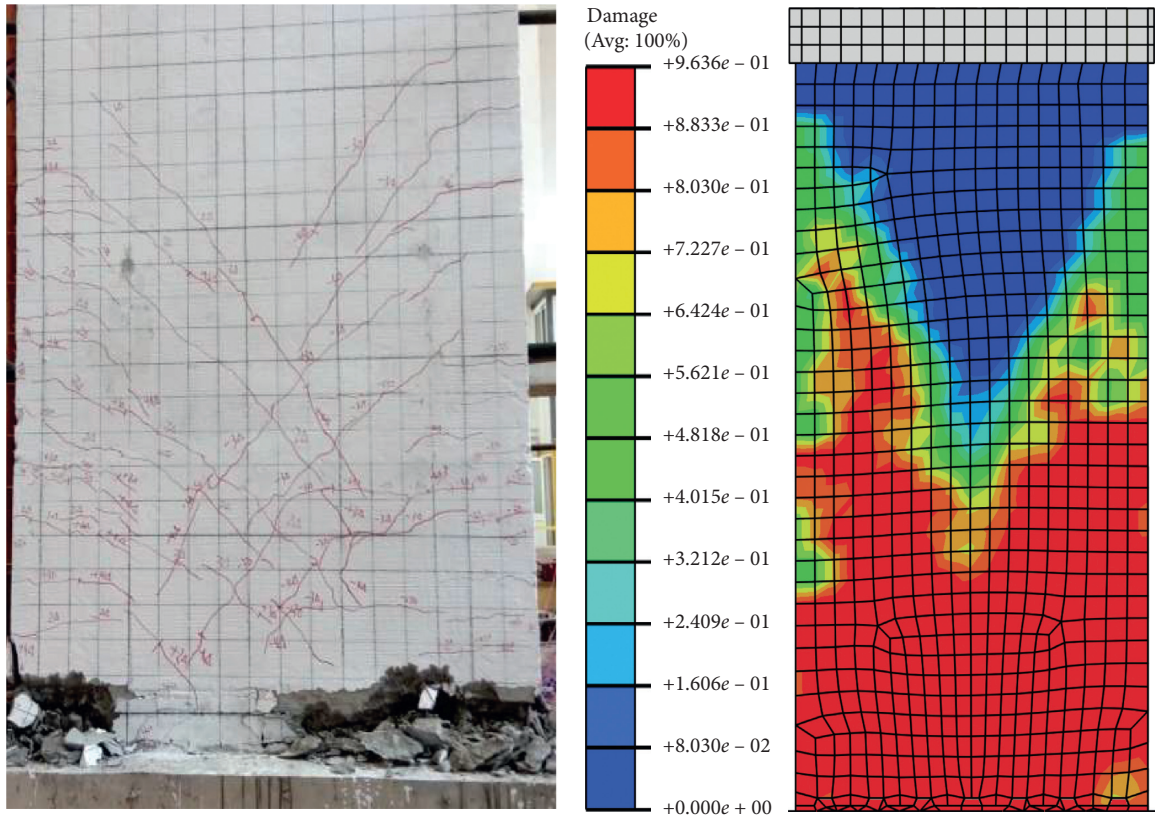

Figure 12: (a) Damage distribution of the test specimen and (b) finite element model. Note: Avg, average.

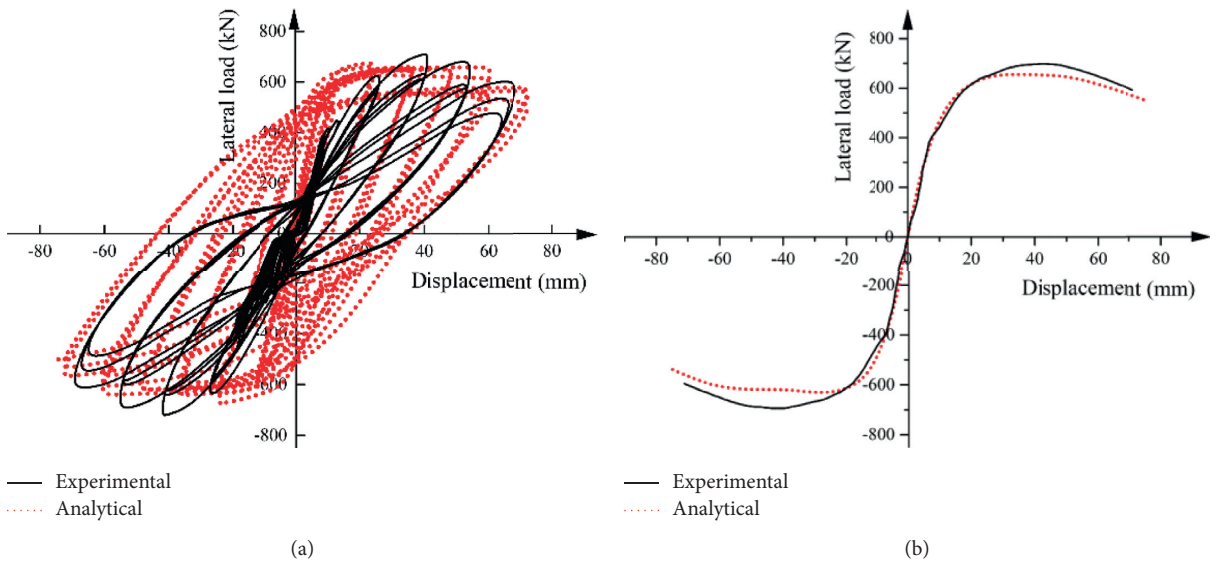

Figure 13: Comparison of simulated and experimental load-displacement curves: (a) hysteresis curves; (b) skeleton curves.

ratio. Meanwhile, the plastic strain of SW1 is concentrated at the bottom of the wall, and the plastic damage area of SW1 is smaller than that of TSW2 with the same shear span ratio.

Figure 16 shows the tensile damage distribution diagram of each specimen. In specimen SW1, significant tensile damage distributes along the bottom to the middle of the wall and the two boundary confinement columns between the middle part and the top beam. However, obvious tensile damage of reinforce tenon joint specimens is mainly concentrated on boundary confinement columns along the height

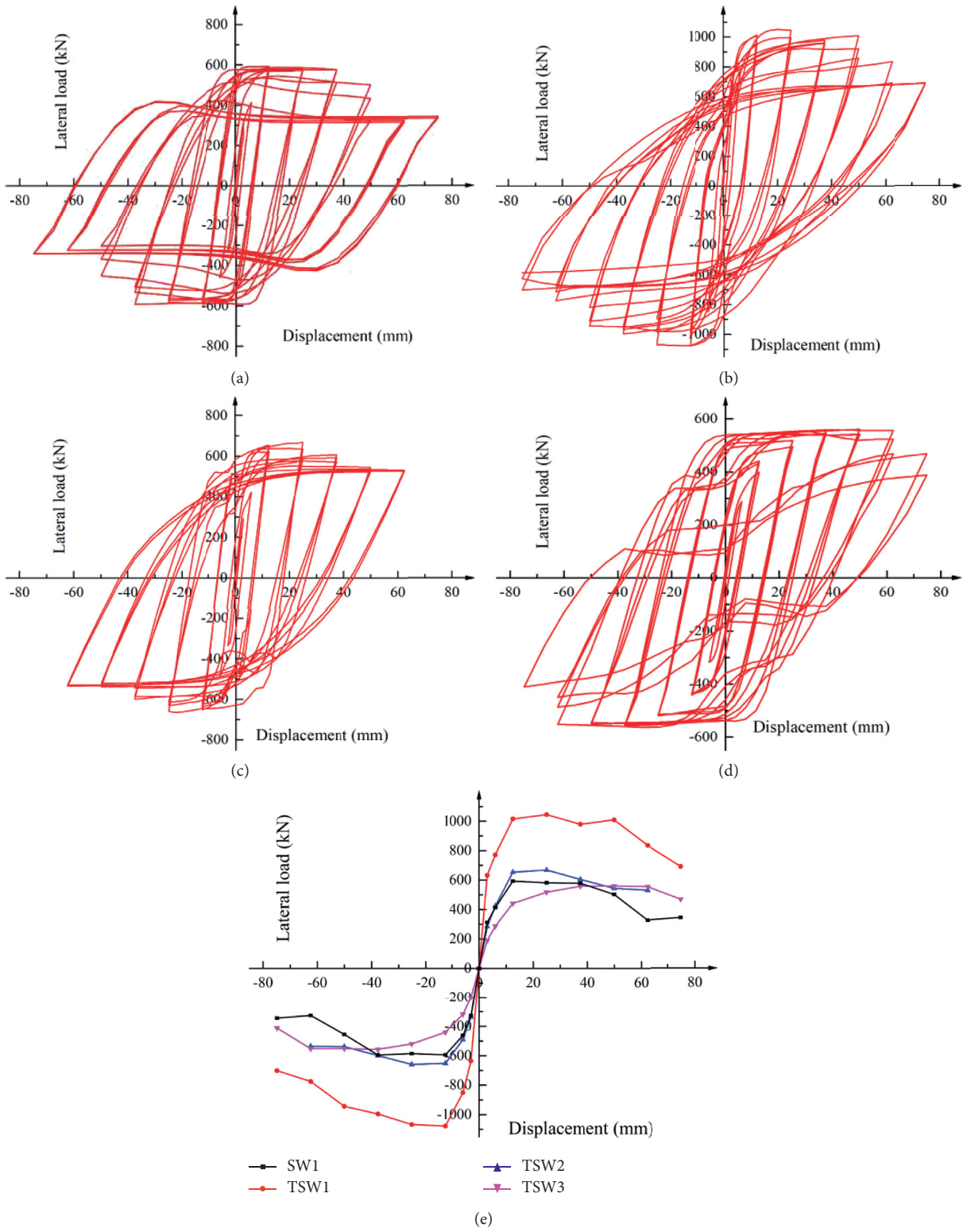

Figure 14: Hysteresis curves of four specimens: (a) SW1; (b) TSW1; (c) TSW2; (d) TSW3; (e) skeleton curves of four specimens.

of the specimen. The potential reason for this is that the vertical distributed connecting bars in the groove are disconnected, so all bending moments are transferred to the boundary confinement columns. Thus, the effect of separating the bending moment and the shearing forces is realized.

It can be seen from Figures 15 and 16 that the damage at the root of the boundary confinement columns is slight. It is probably related to the following: (1) The reinforced tenon bears most of the shear force on the joint interface, so the shear damage on the boundary columns is reduced. (2)

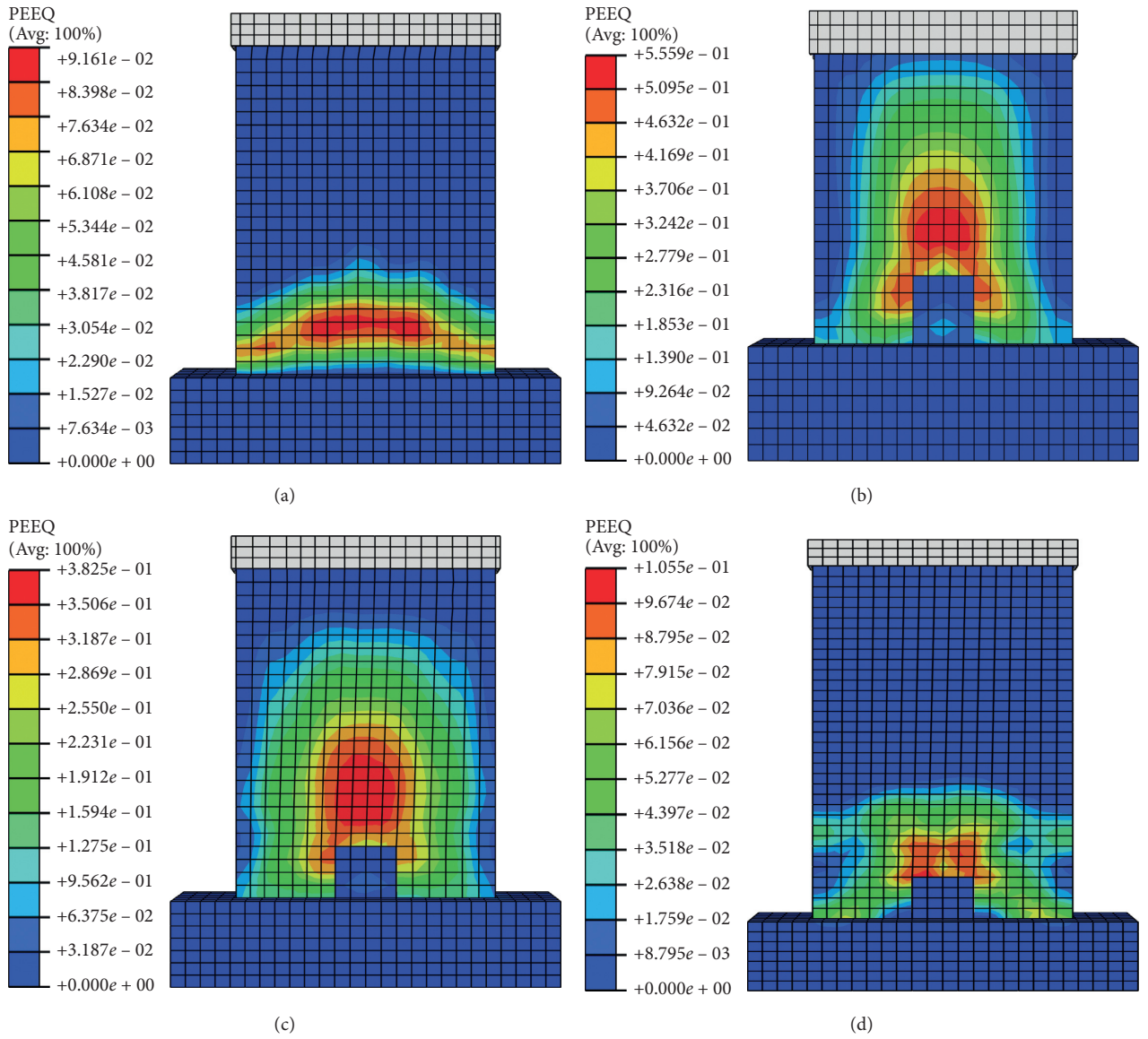

Figure 15: Equivalent plastic strain distribution diagrams of four specimens. (a) SW1. (b) TSW1. (c) TSW2. (d) TSW3. Note: PEEQ, equivalent plastic strain distribution diagram; Avg, average.

Reducing the space of the exterior stirrups to 50 mm further improves the concrete confinement.

3.3. Strength. The strength characteristics of four specimens are listed in Table 3. The values are calculated from the average of the positive and negative directions. Comparing TSW1, TSW2, and TSW3, with the increase of shear span ratio, the yielding, the peak, and the ultimate strength of all three specimens decrease in the sequent. It can be observed that the yielding strength of TSW2 is 526.3 kN, which is 9.4% higher than that of SW1. The peak strength of 634.7 kN of TSW2 is 6.1% higher than that of SW1, and the relevant horizontal displacement of TSW2 under ultimate load is 47.7 mm, which is 5.5 mm higher than that of SW1. Meanwhile, the TSW3 specimen exhibits higher ultimate strengths than that of SW1, even though the TSW3 was subjected to largest shear span ratio. The results indicate that the strength and the ductility of reinforced tenon joint specimens are higher and better than common those of flat-seam joint precast wall.

3.4. Stiffness Degradation. Figure 17 shows the stiffness degradation of the four specimens. The stiffness is determined based on the secant stiffness defined as the averaged slop of the lines connecting the peak positive and the negative response points of the cycles during a load increment. The stiffness at the first cycle of each displacement loading increment is calculated. The stiffness of each wall degrades following the similar trend. The rate of stiffness degradation of shear walls is the fastest from initial to yield, while it is slightly slower at the stage from yield to ultimate.

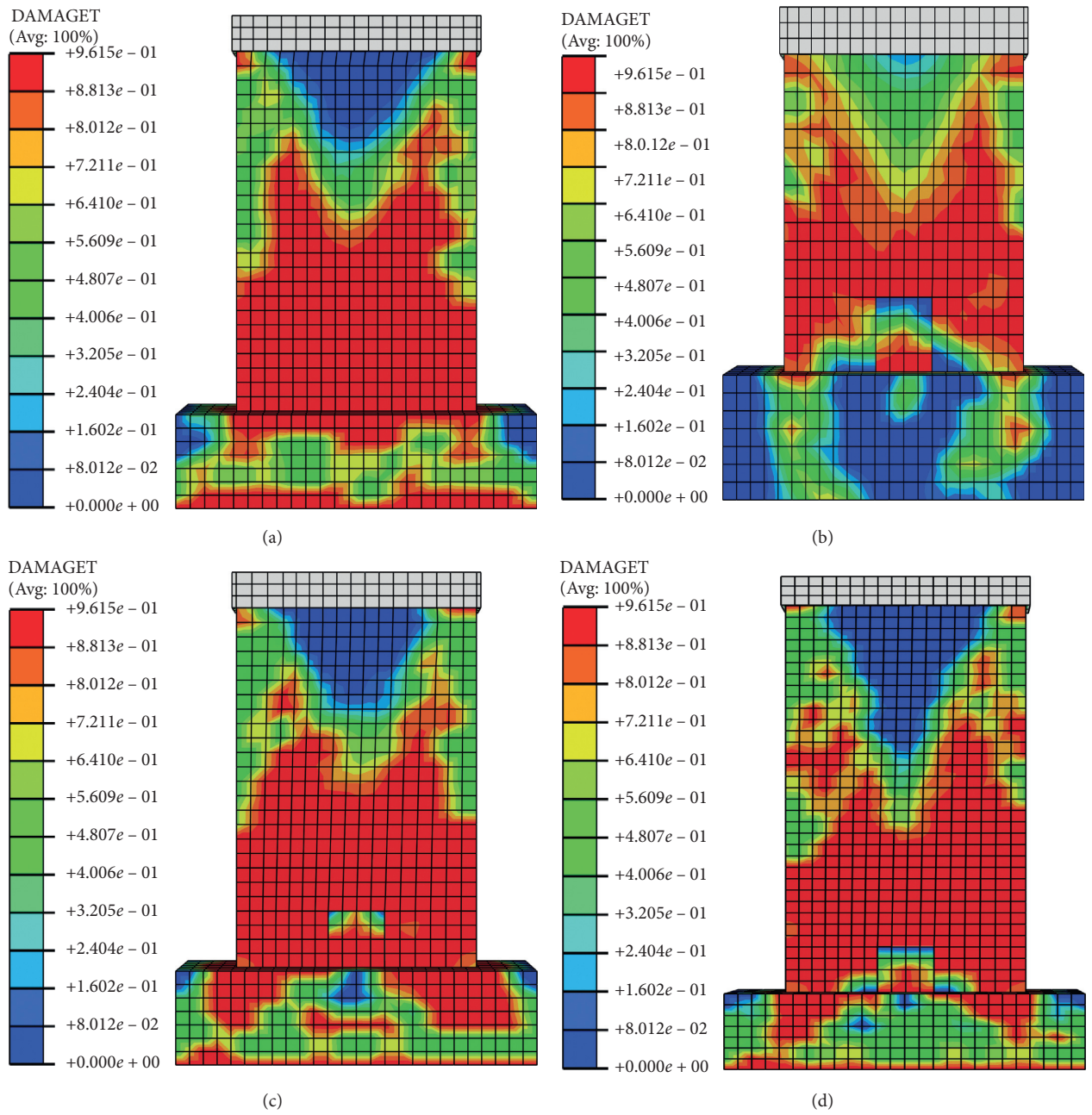

Figure 16: Tensile damage distribution diagrams of four specimens. (a) SW1. (b) TSW1. (c) TSW2. (d) TSW3. Note: DAMAGET, tensile damage distribution diagram; Avg, average.

With increasing shear span ratio of shear walls, the stiffness degradation curve becomes gentle, the initial stiffness decreases, and the rate of stiffness degradation slows down. Specimen TSW2 maintains higher stiffness throughout the test compared with the specimen SW1.

3.5. Displacement Ductility Behavior. The yield displacement, the ultimate displacement, and the displacement ductility coefficients are listed in Table 4. The ductility of the shear walls is evaluated using the displacement ductility coefficient μ calculated as $\mu = \Delta_u/\Delta_y$, where Δ_y is the lateral displacement at yield and Δ_u is the horizontal displacement corresponding to the failure of the wall. The graphic method [23, 26] was adopted to determine the yield point shown in Figure 18. According to the China code for design of concrete structures (GB 50010-2010) [15], the displacement is considered the ultimate displacement when the load drops to 85% of the maximum. The shear span ratio influences the displacement ductility, and with the increase of shear span ratio, the ductility of TSW1, TSW2, and TSW3 decreases in turn. That can be explained by the PEEQ area of three specimens from Figure 15. The plastic damage areas of TSW1 and TSW2 are large and the distributions are even.

Table 3: Strength characteristics of four specimens at different stages.

Specimen	Axial load	Yield stage		Peak stage		Ultimate stage		Ultimate drift ratio
		F_y (kN)	Δ_y (mm)	F_m (kN)	Δ_m (mm)	F_u (kN)	Δ_u (mm)	θ_u
SW1	567.8	481.0	8.5	598.7	12.5	493.9	42.2	1/60
TSW1	567.8	827.6	6.5	1006.0	12.5	855.0	53.8	1/32
TSW2	567.8	526.3	8.5	634.7	12.5	539.5	47.7	1/53
TSW3	567.8	438.0	13.4	554.5	37.4	470.9	67.0	1/51

F_y is the horizontal yield load; F_m is the horizontal peak load; F_u is the horizontal ultimate load; Δ_y is the yield lateral displacement; Δ_m is the peak lateral displacement; Δ_u is the failure lateral displacement.

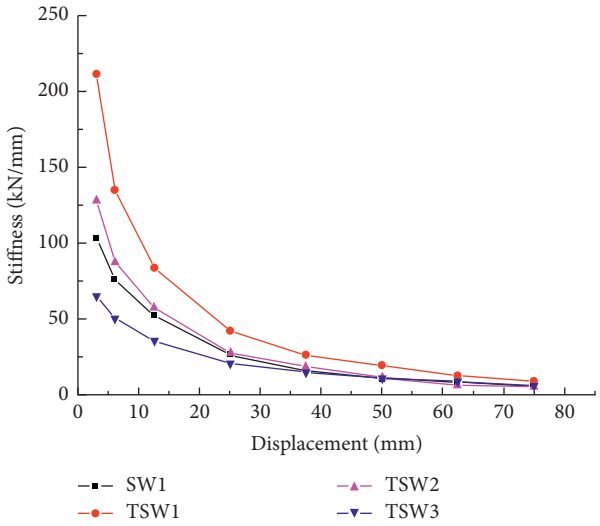

Figure 17: Stiffness degradation of four specimens.

Table 4: Summary of ductility parameters for four specimens.

Specimen	Yield disp., Δ_y (mm)	Ultimate disp., Δ_u (mm)	Ductility coefficient, $\mu = D_u/D_y$	Bearing capacity, F_m (kN)
SW1	8.50	42.20	4.90	698.7
TSW1	6.53	53.77	8.23	1006
TSW2	8.50	47.70	5.61	634.7
TSW3	13.40	67.00	5.00	554.5

However, the plastic damages of TSW3 and SW1 are concentrated at the bottom of the wall. When the concrete and steel elements reach the ultimate stress damage, the wall will be damaged and lose bearing capacity. However, for the specimens with uniform plastic damage distribution, more elements are involved in the stress and can bear more loads. The results show that the reinforced tenon can actively affect the displacement ductility of the precast specimen to a certain extent.

3.6. Energy Dissipation Behavior. The energy dissipation behaviors of the specimens are evaluated using the summation of energy dissipation of each load cycle. The dissipated energy in each cycle is evaluated from the lateral load versus the lateral displacement hysteretic curves, as the area bounded by the hysteretic loop of that cycle. Figure 19

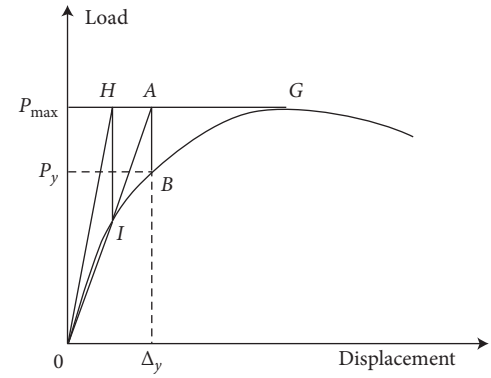

Figure 18: Yield bending moment graphic method.

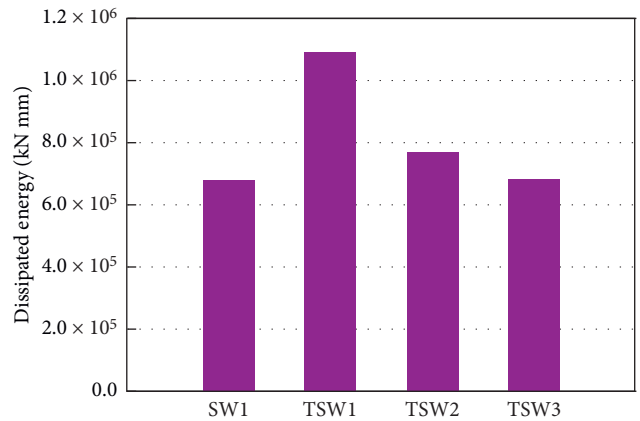

Figure 19: Comparison of total dissipated energies of four specimens.

compares the total dissipated energy within each specimen. The total dissipated energies of specimens TSW1–3 decrease with the increase in the shear span ratio, demonstrating the negative impact of the shear span ratio on the energy absorption capacity of the reinforced tenon precast shear wall. However, due to the reinforced tenon in the joint surface, the staggered slipping can be eliminated after the joint cracks, which improves the mechanical performance of the shear wall, makes the damage in the middle part of the wall more even, and absorbs more energy than the stress concentration failure in the common flat-seam joint specimen. Therefore, specimen TSW2 with the same shear span ratio dissipates more energy than SW1 at the ultimate drift.

4. Bearing Capacity Model of Reinforced Tenon Precast Shear Wall

4.1. Internal Force Composition at the Joint Interface. The crack interface of common flat-seam joint concrete is irregular and rough, and many pairs of complex interaction forces form. However, the reinforced tenon joint specimen is liable to crack along the joint surface and forms a penetrating crack. The arrangement direction of reinforcing bars in the penetrating crack has a regular parallel or orthogonal relationship with the crack. Thus, the stress transfer mechanisms can be simplified as follows: (1) axial tension and compression force on the steel bars, (2) pressure between the concrete interfaces, (3) frictional force related to the axial force, and carried by the concrete interface [22, 27]. According to the failure phenomena, a simplified calculation model for the bearing capacity of the reinforced tenon joint precast shear wall is proposed. Figure 20 shows the distributions of internal force and strain at joint interface.

The fundamental assumptions for model calculation are as follows:

(1) Lap-spliced joint by grouting metal bellow can effectively transfer the reinforcement stress.

(2) The top surface of the reinforced tenon compactly contacts with the bottom surface of the wall panel, which can transmit the compressive stress well, so the joint section conforms to the plane section assumption.

(3) The tensile strength of concrete is neglected, and the influence of stirrup restraint on the concrete is considered.

(4) The constitutive model of the reinforcing bar adopts the ideal elastic-plastic model.

(5) The horizontal shear force at the joint surface is borne by the reinforcement tenon and the friction between the concrete interfaces. The friction coefficient of concrete interface is 0.4 [28].

The calculation sketch of reinforced tenon joint precast shear wall is shown in Figure 21. The height is h_w, and the thickness is b.

In Figure 21(a), l_c is the width of the boundary column. The distances from the resultant force point of longitudinal reinforcement to the corresponding edges of the boundary columns on both sides are a_s and a_s', respectively. Figure 21(b) shows the strain distribution of section. The longitudinal reinforcement at the edge of the boundary column in the tension region reaches the yield strain ε_y, the concrete at the boundary column in the compression region reaches the ultimate compressive strain ε_0, the concrete at the edge of the boundary column in the compression region reaches the ultimate compressive strain ε_c, and x_c is the height of the compressive region of the cross section. Figure 21(c) shows the schematic diagram of reinforcement forces in the boundary columns. T_S and C_S are the tension and the pressure stress of longitudinal reinforcement, respectively. Figure 21(d) shows the stress distribution

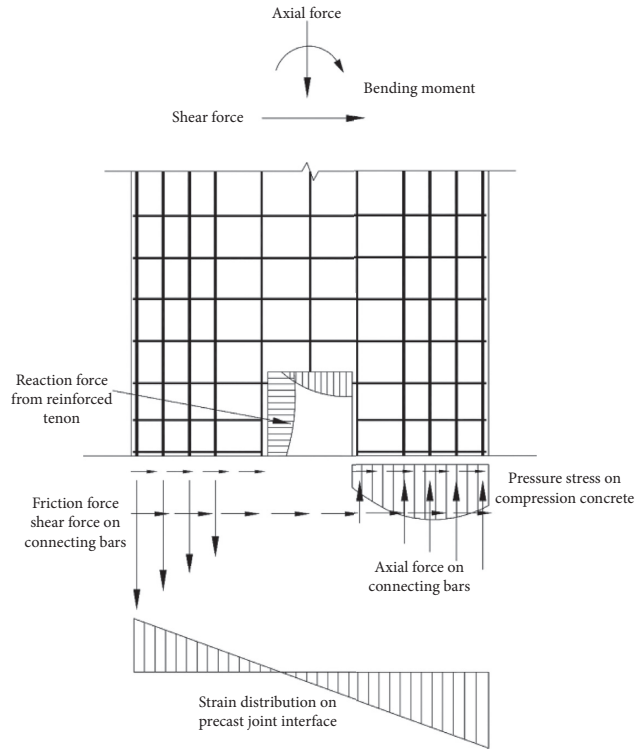

Figure 20: Distributions of internal force and strain at joint interface.

diagram of concrete at the joint interface. C_1 and C_2 are the pressure stresses of unconfined and confined concretes in the boundary column, respectively, and x_b is the height of the compression region of the equivalent rectangular stress block. The concrete in the tension region withdraws from work after cracking.

4.2. Constitutive Relationship of Confined Concrete. The concrete in the boundary column of the shear wall was confined by stirrups. Therefore, the effect of confined stirrups on the bearing capacity of the concrete should be considered. In this paper, the stress-strain constitutive model of confined concrete proposed by Smani and Attard [29] is selected. The compressive strength of confined concrete is as follows:

$$f_0 = f_{ck}\left(\frac{f_{cc}'}{f_{tk}} + 1\right)^{1.25\left(f_{ck}\right)^{-0.21}\left(1+0.062 f_{cc}'/f_{ck}\right)}. \tag{4}$$

The corresponding ultimate compressive strain is

$$\varepsilon_0 = \varepsilon_c\left[1 + \left(17 - 0.006 f_{ck}\right)\left(\frac{f_{cc}'}{f_{ck}}\right)\right], \tag{5}$$

where f_{ck} and f_{tk} are the standard values of axial compressive and axial tensile strengths of concrete, respectively, and f_{cc}' is the confined stress caused by confined reinforcement on concrete. According to Saatcioglu [30], the confined stress f_r can be calculated by using formula (9):

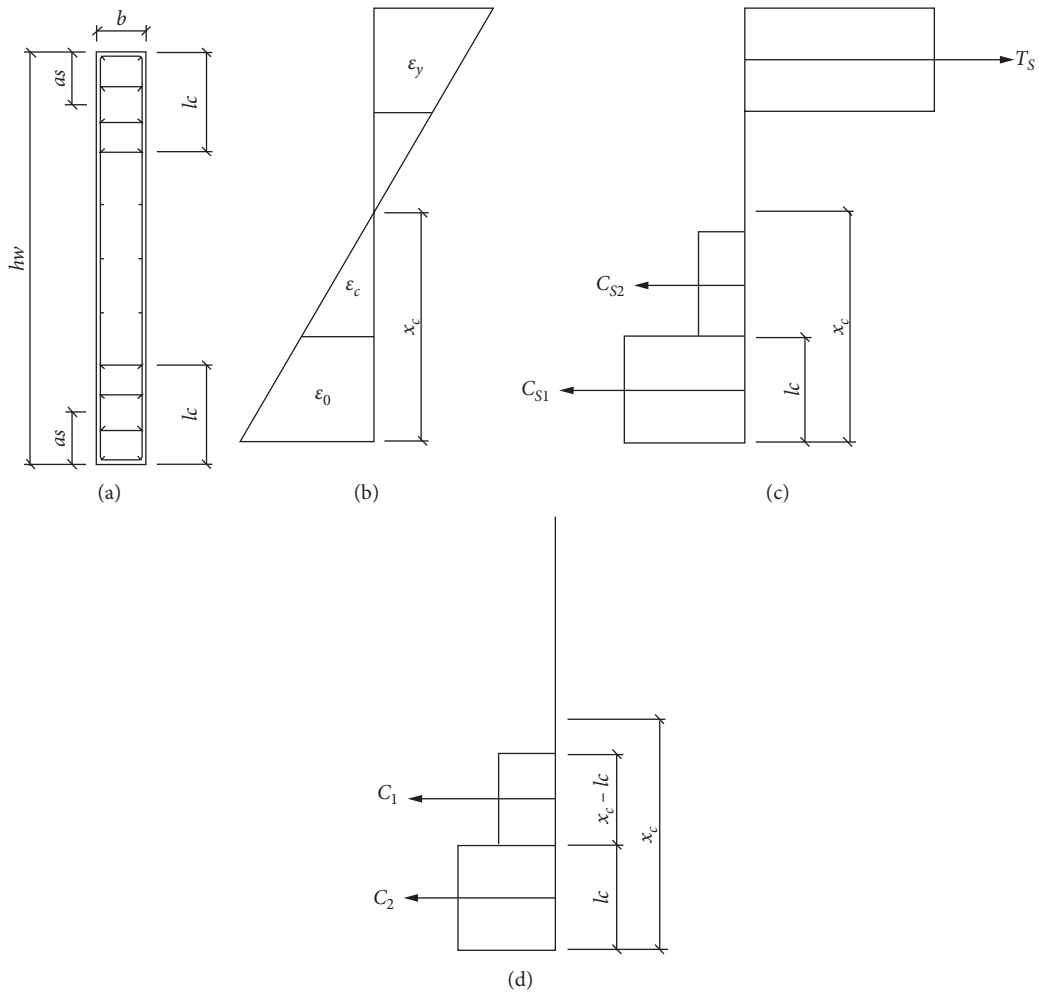

Figure 21: Calculation sketch of reinforced tenon joint precast shear wall. (a) Section size. (b) Strain distribution. (c) Steel stress. (d) Concrete stress.

$$f'_{cc} = 0.26\left[\frac{\rho_{sx} + \rho_{sy}}{s\left(b_{cx} + b_{cy}\right)}\right], \tag{6}$$

$$\rho_{sx} = \sum A_{sx} f_{yt} \sqrt{\left(\frac{b_{cy}}{s}\right)\left(\frac{b_{cy}}{b_{cx}}\right)\left(\frac{1}{f_{yt}}\right)}, \tag{7}$$

$$\rho_{sy} = \sum A_{sy} f_{yt} \sqrt{\left(\frac{b_{cx}}{s}\right)\left(\frac{b_{cx}}{b_{cy}}\right)\left(\frac{1}{f_{yt}}\right)}, \tag{8}$$

where A_{sx} and A_{sy} are the regions of rectangular stirrups in the directions of X and Y, respectively, b_{cx} and b_{cy} are the widths of the stirrups in the directions of X and Y, respectively. S is the vertical spacing of rectangular stirrups, and f_{yt} is the yield strength of confined stirrups.

4.3. Calculation of Compression-Bending Capacity. Since the connection of distributing bars in the joint interface is cancelled, the interfacial forces mainly include unconfined concrete pressure stress C_1, confined concrete pressure C_2, longitudinal reinforcement tension T_S and longitudinal reinforcement pressure C_S. Considering the restraint effect of stirrups, the strength of concrete increases as follows:

$$C_2 = \alpha_1 f_0 b l_c. \tag{9}$$

The strength of unconfined concrete pressure stress is

$$C_1 = \alpha_1 f_c b\left(x_b - l_c\right). \tag{10}$$

According to the boundary columns with symmetrical reinforcements at each side, the vertical bearing capacity of the wall is as follows:

$$N_b = C_2 + C_1, \tag{11}$$

$$N_b = \alpha_1 f_0 b l_c + \alpha_1 f_c b\left(x_b - l_c\right). \tag{12}$$

According to formula (12), the critical compressive height of concrete can be calculated as follows:

$$x_b = \frac{N_b + \alpha_1 b l_c\left(f_c - f_0\right)}{\alpha_1 f_c b}. \tag{13}$$

The bending capacity of the jointed section can be obtained by considering the position of the tension yielding reinforcements as the bending moment center:

Table 5: Comparison of numerical simulation and calculation results.

Specimen	Numerical results V_N (kN)	Calculated value V_C (kN)	Error (%)
TSW1	1006	948.5	5.7
TSW2	634.7	632.3	0.4
TSW3	554.5	474.3	14.5

$$M_b = \alpha_1 f_0 b l_c \left(h_0 - \frac{l_c}{2}\right) + \alpha_1 f_c b (x_b - l_c)\left(h_0 - \frac{(x_b + l_c)}{2}\right) + f_y' A_s' (h_0 - a_s) + N\left(a_s - e_a - \frac{h}{2}\right). \quad (14)$$

The shear forces for the specimens calculated by using formula (14) are listed in Table 5.

Table 5 compares the numerical simulation and calculation results. The errors of specimens TSW1 and TSW2 are small, which shows that the formula is more accurate for the reinforced tenon precast shear wall with small shear span ratio. Moreover, the numerical result of TSW3 is 14.5% higher than the calculated value, which indicates that the disconnection of vertical distribution bars and the setting of reinforced tenon have little effect on the bearing capacity of high shear span ratio specimens. The calculated result of each reinforced tenon specimen is lower than that of the numerical simulation. The main reason is that the shear resistance capacity of the reinforced tenon is neglected when calculating the bearing capacity of the specimen. The reinforced tenon reduces the disturbance of the interface slip on the strength of the vertical connection reinforcements. Thus, when calculating the bearing capacity of components, the advantageous influence of reinforcement tenon can be used as the safety reserve in the design [30].

5. Summary and Conclusions

In this paper, the reinforced tenon joint precast shear wall is proposed. The numerical simulations validate that the proposed reinforced tenon can effectively bear most of the shear force of the joint interface. Bearing capacity model and calculation are also conducted. The following conclusions can be drawn from the results and analysis:

(1) With proper design, the reinforced tenon joint precast shear wall can provide sufficient strength, stiffness, ductility, and energy dissipation. The mechanical performance of the reinforced tenon joint is better than that of common flat-seam joint wall specimen.

(2) As the shear span ratio ranges from 1 to 2, the strength, stiffness, ductility, and energy dissipation decrease in turn. The influence of reinforced tenon on the mechanical properties of the specimen reduces with the increase of shear span ratio.

(3) The boundary columns of common flat-seam joint specimen should bear both bending moment and shearing force. However, the reinforced tenon joint can separate the bending and the shearing forces onto the boundary columns and the reinforced tenon part, respectively. Each component fully utilizes the respective force advantages and improves the capacity of the joint surface.

(4) Compared with the other three specimens, specimen TSW1 has higher bearing capacity and fully developed cracks, which show that the reinforced tenon connections are more suitable for low shear-span ratio shear walls with larger horizontal shear forces at the joint interface.

(5) With the horizontal reaction force from the reinforced tenon, the steel tension stress concentrates on the top of the joint gap and forms a new weak point. The reinforcement at the gap will be enhanced in the future study. Furthermore, the effects of the reinforcement ratio of the boundary confinement column and the size of the reinforced tenon will be studied in the future study.

Data Availability

The data used to support the findings of this study are available from the corresponding author upon request.

Conflicts of Interest

The authors declare that they have no conflicts of interest.

Acknowledgments

This work has received financial support from the National Natural Science Foundation for Young Scientists of China (Grant no. 51708260), Postgraduate Research & Practice Innovation Program of Jiangsu Province (SJCX19_0620), the University Natural Science Foundation funded by the Jiangsu Provincial Government (Grant no. 2016TM045J), the Natural Science Fund of Jiangsu (BK20141090), and the Suzhou Science and Technology Project (SNG201904).

References

[1] I. N. Psycharis, I. M. Kalyviotis, and H. P. Mouzakis, "Experimental investigation of the response of precast concrete cladding panels with integrated connections under monotonic and cyclic loading," *Engineering Structures*, vol. 159, pp. 75–88, 2018.

[2] Y.-R. Dong, Z.-D. Xu, K. Zeng, Y. Cheng, and C. Xu, "Seismic behavior and cross-scale refinement model of damage evolution for RC shear walls," *Engineering Structures*, vol. 167, pp. 13–25, 2018.

[3] X. Lu, L. Wang, D. Wang, and H. Jiang, "An innovative joint connecting beam for precast concrete shear wall structures," *Structural Concrete*, vol. 17, no. 6, pp. 972–986, 2016.

[4] Q. Jiaru, P. Yuanyuan, Z. Jingming et al., "Tests on seismic behavior of pre-cast shear walls with vertical reinforcements spliced by grout sleeves," *Building Structures*, vol. 2, pp. 1–6, 2011.

[5] Q. Jiaru, Y. Xinke, Q. Heng et al., "Tests on seismic behavior of pre-cast shear walls with various methods of vertical

reinforcement splicing," *Journal of Building Structures*, vol. 6, pp. 51–59, 2011.

[6] J. H. Ling, A. B. Abdul Rahman, I. S. Ibrahim, and Z. Abdul Hamid, "Behaviour of grouted pipe splice under incremental tensile load," *Construction and Building Materials*, vol. 33, no. 3, pp. 90–98, 2012.

[7] M. Soltani, X. An, and K. Maekawa, "Computational model for post cracking analysis of RC membrane elements based on local stress-strain characteristics," *Engineering Structures*, vol. 25, no. 8, pp. 993–1007, 2003.

[8] D.-Y. Wu, S.-T. Liang, Z.-X. Guo, and X.-J. Zhu, "Flexural capacity calculation approach for precast grouted shear wall influenced by joint interface displacements," *Advances in Materials Science and Engineering*, vol. 2015, Article ID 120759, 11 pages, 2015.

[9] M. Soltani, X. An, and K. Maekawa, "Localized nonlinearity and size-dependent mechanics of in-plane RC element in shear," *Engineering Structures*, vol. 27, no. 6, pp. 891–908, 2005.

[10] D. Wu, S. Liang, M. Shen, Z. Guo, X. Zhu, and C. Sun, "Experimental estimation of seismic properties of new precast shear wall spatial structure model," *Engineering Structures*, vol. 183, pp. 319–339, 2019.

[11] H. R. Foerster, S. H. Rizkalla, and J. S. Heuvel, "Behavior and design of shear connections for loadbearing wall panels," *PCI Journal*, vol. 34, no. 1, pp. 102–119, 1989.

[12] K. A. Soudki, S. H. Rizkalla, and B. LeBlanc, "Horizontal connection for precast concrete shear walls subjected to cyclic deformations part 1: mild steel connections," *PCI Journal*, vol. 40, no. 4, pp. 78–96, 1995.

[13] Z. Xizhi, T. Jiesong, C. Weiwei et al., "Influence of embedded-column ratio of longitudinal reinforcement on compression-bending behavior of prefabricated shear wall with tooth-grooved connection," *Building Structure*, vol. 10, pp. 24–31, 2016.

[14] Z. Xizhi, M. Jian, H. Peng et al., "Shear behavior on pre-fabricated shear wall alveolar type connection," *Journal of Building Structures*, vol. 11, pp. 93–100, 2017.

[15] GB50010–2010, code for design of concrete structures, 2015(10):28-30.

[16] Z. Zhanting and L. Yufeng, "Concrete damaged plasticity model in abaqus," *Building Structure*, vol. 2, pp. 229–231, 2011.

[17] Q. Wu, X. Li, J. Xu, G. Wang, W. Shi, and S. Wang, "Size distribution model and development characteristics of corrosion pits in concrete under two curing methods," *Materials*, vol. 12, no. 11, p. 1846, 2019.

[18] H. D. Hibbitt, *Abaqus User's Manual*, Dassault Systemes Simulia, Providence, RI, USA, 2011.

[19] R. Yin, C. Zhang, Q. Wu, B. Li, and H. Xie, "Damage on lining concrete in highway tunnels under combined sulfate and chloride attack," *Frontiers of Structural and Civil Engineering*, vol. 12, no. 3, pp. 331–340, 2018.

[20] R. Yin, J. Hu, Y. Liu, Q. Wu, C. Zhang, and Y. Wang, "Study on corrosion effect of high-performance concrete under the action of sulfate and chlorine," *International Journal of Modern Physics B*, vol. 33, no. 3, Article ID 1940054, 2019.

[21] S. Chongfang, *Study on Seismic Performance of Prefabericated Shear Wall with Rabbet-Unbonded Horizontal Connection*, Southeast University, Nanjing, China, 2017.

[22] P. M. D. Santos and E. N. B. S. Júlio, "A state-of-the-art review on shear-friction," *Engineering Structures*, vol. 45, no. 15, pp. 435–448, 2012.

[23] F. Peng, Q. Han-Lin, and Y. Lie-Ping, "Discussion and definition on yield points of materials, members and structures," *Engineering Mechanics*, vol. 3, pp. 36–46, 2017.

[24] D. Wu, S. Liang, M. Shen et al., "Finite-element simulation on NPGCS precast shear wall spatial structure model," *Advances in Civil Engineering*, vol. 2019, Article ID 2647891, 17 pages, 2019.

[25] C. Sun, S. Liang, X. Zhu, Y. Song, and D. Wu, "Ductility calculation of prefabricated shear wall with rabbet-unbond horizontal connection," *Advances in Civil Engineering*, vol. 2018, Article ID 5197125, 12 pages, 2018.

[26] Z. Guo and S. Xudong, *Reinforced Concrete Theory and Analyse*, Tsinghua University Press, Beijing, China, 2003.

[27] K. Zilch and R. Reinecke, "Capacity of shear joints between high-strength precast elements and normal-strength cast-in-place decks," in *Proceedings of the International Symposium on High Performance Concrete*, pp. 25–27, Orlando, FL, USA, Seeptember 2000.

[28] S. G. Tsoukantas, "Shear resistance of connections between reinforced concrete linear precast elements," *ACI Structural Journal*, vol. 86, no. 3, pp. 242–249, 1989.

[29] A. K. Samani and M. M. Attard, "A stress-strain model for uniaxial and confined concrete under compression," *Engineering Structures*, vol. 41, no. 3, pp. 335–349, 2012.

[30] M. Saatcioglu, "Strength and ductility of confined concrete," *Journal of Structural Engineering*, vol. 118, no. 6, pp. 1590–1607, 1992.